Transonic Shock Oscillations and Wing Flutter Calculated with an Interactive Boundary Layer Coupling Method

John W. Edwards
NASA Langley Research Center
Hampton, Virginia USA

EUROMECH-Colloquium 349
Simulation of Fluid-Structure Interaction in Aeronautics
Göttingen, Germany
September 16–18, 1996

TRANSONIC SHOCK OSCILLATIONS AND WING FLUTTER CALCULATED WITH AN INTERACTIVE BOUNDARY LAYER COUPLING METHOD

John W. Edwards*
NASA Langley Research Center
Hampton, Virginia USA 23681-0001

Abstract

A viscous-inviscid interactive coupling method is used for the computation of unsteady transonic flows involving separation and reattachment. A lag-entrainment integral boundary layer method is used with the transonic small disturbance potential equation in the CAP-TSDV code. Efficient and robust computations of steady and unsteady separated flows, including steady separation bubbles and self-excited shock-induced oscillations are presented. The buffet onset boundary for the NACA 0012 airfoil is accurately predicted and shown computationally to be a Hopf bifurcation. Shock-induced oscillations are also presented for the 18 percent circular arc airfoil. The oscillation onset boundaries and frequencies are accurately predicted, as is the experimentally observed hysteresis of the oscillations with Mach number. This latter stability boundary is identified as a jump phenomenon. Transonic wing flutter boundaries are also shown for a thin swept wing and for a typical business jet wing, illustrating viscous effects on flutter and the effect of separation onset on the wing response at flutter. Calculations for both wings show limit cycle oscillations at transonic speeds in the vicinity of minimum flutter speed indices.

Introduction

The onset of transonic shock-induced flow separation is known to be associated with a variety of nonclassical aeroelastic instability and response phenomena,[1-3] referred to variously as; single degree of freedom flutter, limited-amplitude flutter, limit cycle oscillations (LCO), control surface buzz, and buffeting (onset). A characteristic of the "instabilities" involved is a tendency to grow to a constant or bounded "limit amplitude" which can vary from a nuisance level to levels large enough to cause structural failure. In the latter case, the nonclassical response, generically referred to herein as LCO, is typically observed near the flutter boundary, making a distinction between the two response mechanisms difficult. Edwards[4,5] reviewed these features of transonic aeroelasticity, concluding that i.) computational capability for such cases would require modeling of dynamically separating and reattaching viscous boundary layers and ii.) such capability was not yet mature for wings or more complete configurations.

Transonic separation can also lead to the occurrence of self-excited shock-induced oscillations (SIO) for perfectly rigid structures; well documented in the case of two-dimensional (2-D) airfoils.[6-10] The unsteady airloads generated are quite large, occur for narrow ranges of transonic Mach number (and angle of attack), and have characteristic frequencies which can be near those involved in flutter. The ability to calculate SIO conditions may be necessary in order to treat the LCO phenomena. Refs. 10–12 report calculations of SIO using 2-D unsteady Navier-Stokes codes. While shock oscillations were obtained, the calculations were sensitive to detailed modeling issues (wind tunnel geometry, grid spacing, etc.), computed frequencies tended to be low, and results were given only for isolated conditions within the interior of SIO regions. More recent calculations of SIO for these two airfoils are given in Refs. 13–15 where very good agreement with SIO onset boundaries and frequencies are obtained.

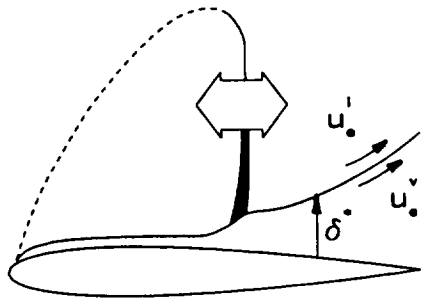

Fig. 1 Sketch of shock-boundary layer interaction.

Interactive Boundary Layer Modeling (IBLM) provides an alternative to such direct computation of flows involving viscous shear layers. Separate computations are made for an inner viscous boundary layer region and an outer inviscid flow region as illustrated in Fig. 1. Subscript "e" denotes the "edge" of the boundary layer, while superscripts "i" and "v" denote inviscid and viscous variables. Ref. 16 developed an integral boundary layer lag-entrainment method to compute displacement thickness δ^* which was used to update the flow tangency boundary condition of the inviscid solver. This "direct" solution

*Senior Research Engineer, Aeroelasticity Branch, Structures Division

method for the entrainment equation becomes singular at flow separation and "inverse" computation methods[17-22] have been developed in attempts to treat flow separation. Carter[17] introduced an iterative, relaxation method for coupling the inner and outer region edge velocities for steady flows. Melnik and Brook[18] incorporated the free shear layer closure modeling of Ref. 19 into their steady inverse lag-entrainment method, using Carter's[17] coupling method to interact with a steady full potential code. Results[18] indicate that only small regions of separated flow could be treated. LeBalleur and Girodroux-Lavigne[19] developed a semi-implicit method for coupling unsteady boundary layer and Transonic Small Disturbance (TSD) potential equations, showing examples of transonic separated flow including SIO conditions. Unsteady lag-entrainment boundary layer and TSD equations were also coupled in Refs. 20 and 21 using a "quasi-simultaneous" method. Although cases involving separated flow on oscillating airfoils are reported, no examples of SIO calculations are given. Both of these unsteady interactive methods[19, 21] rely upon explicit boundary condition treatment available during the final z-sweep of the 2-D Alternating-Direction Implicit (ADI) solution algorithm. Locally linear relations between the inner and outer flow variables are developed and pointwise iterations with relaxation are used. Bartels[14, 15] has recently developed an IBLM with a fully unsteady finite-difference boundary layer model and presents many SIO calculations.

References 23–27 present further examples of steady IBLM coupled with steady potential and Euler equation solvers. The 2-D transonic separated flow cases shown involve separation onset; shock-induced separation bubbles and trailing-edge separation. Comparisons[23, 24] indicate the IBLM solutions are quite competitive with Navier-Stokes solutions.

Howlett[28]developed an IBLM coupled with the CAP-TSD[29] (Computational Aeroelasticity Program – Transonic Small Disturbance) potential equation code. Howlett's modification of Rizzetta's[30] quasi-steady, direct, lag-entrainment IBLM was incorporated in the CAP-TSD code in a stripwise fashion. Further modifications[31] involved an inverse solution procedure using Carter's coupling method. Experience in calculating unsteady separated transonic flows was similar to that noted above for steady conditions; only small amounts of flow separation could be treated without code failure.

Edwards[32] reported a new coupling method, using Howlett's inverse solution procedure, capable of treating transonic SIO conditions for airfoils. The new coupling method was based upon the observation that at the transonic flow conditions of interest, the flowfield is frequently inherently unsteady with oscillating shocks and dynamically separating and reattaching boundary layers. The IBLM is thus regarded as a simulation of two dynamic systems, the outer inviscid flow and the inner viscous flow, whose coupling requires active control elements in order to minimize the coupling error between the two systems. Reference 32 gives details of this development and calculations of two types of self-excited shock oscillations about rigid airfoils. This paper summarizes these SIO calculations for the NACA 0012 and for the 18 percent thick circular arc airfoils. The extention of the method implemented in the three-dimensional code in a stripwise fashion and termed the CAP-TSDV code, is described below. Calculations of wing flutter are presented for two cases: a 4 percent thick wing flutter model, and a thicker typical business jet wing flutter model.

Mathematical Method

Details of the inviscid flow equation, the boundary layer equations, the modifications to boundary conditions, and the IBLM coupling procedure are summarized in this section. Further details are given in Ref. 32.

Inviscid Flow Equation

The CAP-TSD potential equation code is used in this analysis. The CAP-TSD code uses an approximate factorization algorithm for time-accurate solution of the unsteady TSD equation[29]

$$\frac{\partial f_0}{\partial t} + \frac{\partial f_1}{\partial x} + \frac{\partial f_2}{\partial y} + \frac{\partial f_3}{\partial z} = 0 \qquad (1)$$

where ϕ is the inviscid-disturbance velocity potential and

$$f_0 = -A\phi_t - B\phi_x \qquad (2a)$$

$$f_1 = E_1\phi_x + F_1\phi_x^2 + G_1\phi_y \qquad (2b)$$

$$f_2 = \phi_y + H_1\phi_x\phi_y \qquad (2c)$$

$$f_3 = \phi_z \qquad (2d)$$

where $A = M^2$, $B = 2M^2$, $E_1 = 1 - M^2$, $F_1 = -\frac{1}{2}[3 - (2-\gamma)M^2]M^2$, $G_1 = -\frac{1}{2}M^2$, and $H_1 = -M^2$. For the 2-D version of the code, $f_2 = G_1 = 0$. The code contains modifications to these coefficients developed by Batina[33] to approximate the effects of shock generated entropy and vorticity.

The boundary conditions on the airfoil/wing and wake are

$$\phi_z^{\pm} = S_x^{\pm} + S_t^{\pm} \quad ; \quad x_{le} \le x \le x_{te},\ z = 0^{\pm} \qquad (3)$$

$$\Delta\phi_z = 0 \quad ; \quad x > x_{te},\ z = 0^{\pm} \qquad (4)$$

$$\Delta(\phi_x + \phi_t) = 0 \quad ; \quad x > x_{te},\ z = 0^{\pm} \qquad (5)$$

where the superscript $\pm$ refers to the airfoil upper and lower surface, $S(x,t)$ $(S(x,y,t))$ denotes the airfoil (wing) shape, and $\Delta(\cdots)$ indicates the jump in $(\cdots)$ across the wake. Nonreflecting far-field boundary conditions are also used. There have been extensive applications of the 3-D code for unsteady aerodynamic and flutter analysis of wings and complete configurations.[29, 34, 35]

Lag-Entrainment Boundary Layer Equations

The effect of a turbulent viscous boundary layer is modeled in the quasi-steady manner of Green et al.[16] by solving a set of ordinary differential equations in x for the integral boundary layer quantities: momentum thickness θ; shape factor $\overline{H}$; and entrainment coefficient C_E

$$\frac{d}{dx}(\theta) = \frac{1}{2}C_f - (H + 2 - M_e^2)\theta\phi^i_{xx,e} \tag{6}$$

$$\theta\frac{d\overline{H}}{dx} = \left(C_E - \frac{1}{2}H_1 C_f\right)\frac{d\overline{H}}{dH_1} + H_1(H+1)\frac{d\overline{H}}{dH_1}\theta\phi^i_{xx,e} \tag{7}$$

$$\theta\frac{dC_E}{dx} = F\left\{\frac{2.8}{H+H_1}\left[(C_\tau)_{EQO} - \lambda C_\tau^{1/2}\right] + \left(\frac{\theta}{u_e^v}\frac{du_e^v}{dx}\right)_{EQ} - \left[1 + .075M_e^2\frac{1+\frac{\gamma-1}{2}rM_e^2}{1+0.1M_e^2}\right]\theta\phi^i_{xx,e}\right\} \tag{8}$$

Equation (8) is taken from Ref. 19 and differs slightly from that given in Ref. 16. The subscript e refers to quantities at the edge of the boundary layer and the inviscid surface velocity gradient ϕ_{xx} is obtained from the outer flow solver. The various closure parameters in these equations are given in Ref. 31. Equations (6–8) are suitable for attached flow boundary layers and provide the boundary layer displacement thickness

$$\delta^* = H\theta \tag{9}$$

This provides a "direct" calculation of the viscous modification to the airfoil shape to be implemented in the boundary conditions discussed below.

Viscous Boundary Conditions and Wake

The coupling between the inner and outer solutions is through the boundary conditions on the airfoil/wing and wake. Equations (3) and (4) are modified as follows:

$$\phi_z^{\pm} = S_x^{\pm} + S_i^{\pm} + \delta_x^* \;;\; x_{le} \le x \le x_{te},\; z = 0^{\pm} \tag{10}$$

$$\Delta\phi_z = \Delta(\delta_x^*) \;;\; x > x_{te},\; z = 0^{\pm} \tag{11}$$

Viscous Equations for Separated Flow

Correlations of the IBLM equations given above with experiment indicate the onset of flow separation occurs at conditions where $\overline{H} \approx 2.0 - 2.3$ and $C_f \approx 0$. At these values of $\overline{H}$, Eqs. (6–8) become singular ($d\overline{H}/dH_1$ becomes infinite), and alternative solution procedures are necessary. The present study utilizes the "inverse" IBLM as implemented by Howlett,[31] which closely follows that of Melnik and Brook.[18] Eqs. (6–7) are inverted to provide solutions for $\overline{H}_x$ and $u^v_{e_x}$ as functions of the boundary layer displacement thickness, represented by a perturbation mass flow parameter $\overline{m} = \rho_e^i u_e^i \delta^*$. Equation (8) remains unchanged, giving symbolically

$$\frac{du_e^v}{dx} = F_1 + F_2\frac{1}{\overline{m}}\frac{d\overline{m}}{dx} \tag{12}$$

$$\frac{d\overline{H}}{dx} = F_3 + F_4\frac{1}{\overline{m}}\frac{d\overline{m}}{dx} \tag{13}$$

$$\frac{dC_E}{dx} = \frac{1}{\theta}(F_5 + F_6\phi^i_{xx,e}) \tag{14}$$

The F_i variables are nonlinear functions of the parameters modeling the closure conditions for attached and separated flow and are defined in Ref. 31. For separated flows, these closure conditions are based upon the work of Melnik and Brook,[18] which closely follows the development of LeBalleur and Girodroux-Lavigne,[19] where additional details may be found.

Numerical Implementation

From the leading edge of the airfoil, the boundary layer is approximated by the turbulent boundary layer on a flat plate. At a specified point, numerical integration of Eqs. (12–14) is implemented with a fourth-order Runge-Kutta method. For the Mach number range studied, it was found that the inverse equations, in conjunction with the coupling method described below, converged rapidly for attached flow upstream of regions of flow separation (and also for downstream regions of reattached flow). This obviated the use of Eqs. (6–8) thus circumventing the numerically troublesome switching between the direct and inverse equations in separating flow regions, where the largest parameter gradients occur.

Interactive Boundary Layer Coupling Method

Since the intended applications of the IBLM include cases of wing flutter, including SIO and LCO, the coupling method was developed based on the observation that at the transonic flow conditions of interest, the flowfield is frequently inherently unsteady, displaying oscillating shocks and separating and reattaching boundary layers. The interacting boundary layer method is thus regarded as a simulation of two dynamic systems, the outer inviscid flow and the inner viscous flow, whose coupling requires active control elements in order to minimize the coupling error between the two systems. The elements utilized, illustrated in analog block diagram fashion in Fig. 2, include a variable gain integral control element for the displacement thickness and a first order smoothing filter for the momentum thickness estimate. The coupling equations are thus

$$e(x) = u_e^v(x) - u_e^i(x) = u_e^v(x) - \phi^i_{x,e}(x) \tag{15}$$

$$\frac{d\delta^*}{dt} = K_\delta K_1(\delta^*)e \tag{16}$$

$$\frac{d\theta}{dt} = -a\left(\theta(x) - \frac{\delta^*(x)}{H(x)}\right) \tag{17}$$

Equations (17–19) are treated as ordinary differential equations in time at each spanwise location and are implemented using digital filtering methods. The nonlinear gain, $K_1(\delta^*)$, is scheduled on the local displacement thickness in order to enhance the abilitiy of the coupling method to follow moving "wedge-shaped" separated flow regions. Smooth blending of the attached and separated flow closure relations over the range $1.5 < \overline{H} < 2.5$ is implemented via linear interpolation. Finally, the displacement thickness in the wake was modeled to have exponential decay. Numerical experiments[32] indicated relative insensitivity of SIO solutions to the parameters of the wake modeling.

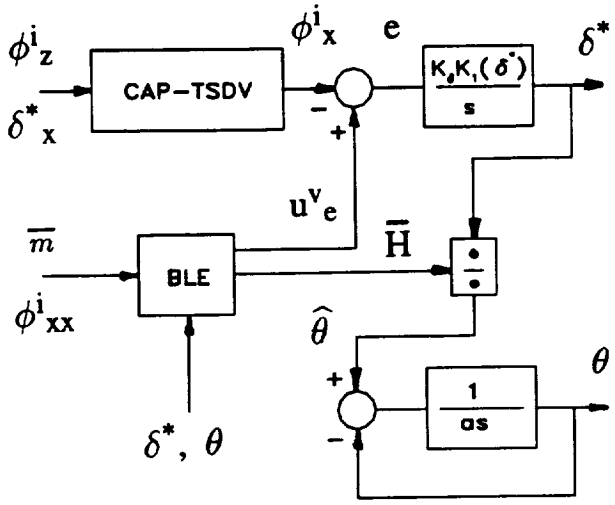

Fig. 2 Schematic diagram of variable gain, integral control, viscous-inviscid interative coupling method.

For the 3–D CAP-TSDV code, Eqs. 12–14 and 15–17 are solved independently at each spanwise chord station on the wing. This is accomplished at each time step, within the Newton linearization iteration loop of the approximate factorization solution algorithm of the CAP-TSD code[36].

Model Descriptions and Results

Airfoil Models

Calculations with the variable gain integral control coupling method are shown for two airfoils and two wing flutter models. The NACA 0012 airfoil and the 18% thick circular arc airfoil demonstrate cases of steady shock-induced separation bubbles, steady trailing-edge separation, and SIO for rigid airfoils. Extensive experimental results have been published for both airfoils and particular attention is drawn to the reports of McDevitt and Okuno[8] and McDevitt.[6,7] For both airfoils, the wind tunnel walls were contoured in order to approximate steady free-air streamline flow (wall boundary layer mass removal using suction was also utilized for the NACA 0012 tests) and regions of Mach number and angle of attack for the onset and quenching of SIO are reported.

The airfoil calculations were obtained on a 212×100 grid in $x-z$ space. The grid extends ± 20 chords in x and ± 25 chords in z. On the airfoils, 146 grid points were distributed in order to capture the large shock excursions involved in SIO: aft of midchord a uniform spacing of 0.5 percent chord was used; forward of 40 percent chord the uniform spacing was $1\frac{1}{3}$ percent chord.

NACA 0012 Airfoil Calculations

Reference 8 reports results from tests of the NACA 0012 airfoil for Mach numbers from approximately 0.7 to 0.8 and at angles of up to six degrees, sufficient to induce buffet onset. Reynolds number based on chord, Re_c, ranged from 1 to 14 million. The test section utilized flexible upper and lower walls, including boundary layer suction, in order to minimize wall interference and provide contouring compatible with free air streamlines. The onset of unsteady "buffet" flow is shown to occur along a well defined boundary of Mach number vs. angle of attack. The pressure waveforms in the buffet region were erratic at low Reynolds number, but for the higher Reynolds numbers well developed cyclic shock oscillations were seen.

Calculations have been made with the 2–D version of CAP–TSDV for steady conditions just below the buffet onset boundary and for SIO conditions at and well beyond the boundary. Results were obtained for time steps of $\Delta t = 0.05$ and for $Re_c = 10$ million. Unless otherwise noted, the inverse IBLM was initiated at 10 percent chord, $K_\delta = 0.00010$, and 5 Newton iterations were performed. Figure 3a compares calculated and experimental surface pressures for $M = 0.775$ and $\alpha = 2.05°$. (Data Set 5 of Ref. 8). The agreement is very good, capturing the pressure levels, shock location, and separation bubble at the foot of the shock. Calculated boundary layer parameters, Fig. 3b, indicate the rapid growth of δ^* through the shock and the effect of the separation bubble is clearly seen in C_f.

Calculations shown in Fig. 4 indicate a well-defined buffet onset boundary in excellent agreement with the experimental boundary.[8] The present results are an improvement over those of Ref. 37, which indicated onset to occur approximately 0.5 degrees higher than experiment. Also, the CAP—TSDV code is able to compute the onset boundary for 0°, where the shock excursion amplitude is largest.

Figure 5 shows the development of the SIO from "zero" flow field conditions for $M = 0.775$ and $\alpha = 4.0°$. While a dominant SIO frequency of $k_b = 0.25$ (based on semichord) can be seen, the lift coefficient exhibits significant nonlinearity.

The development of the SIO with increasing angle of attack shows a Hopf bifurcation onset characteristic, illustrated in Fig. 6. The peak-to-peak oscillation amplitude of the lift coefficient bifurcates at $\alpha = 2.3°$. The amplitude grows quickly to a maximum of 0.3 while the

SIO frequency remains rather constant. Further penetration of the buffet region, to $\alpha = 4.0$ deg., leads to increasing frequency, in good agreement with experiment[8]. The bifurcation amplitude curve is reversible, with the same amplitudes being obtained for decreasing angles.

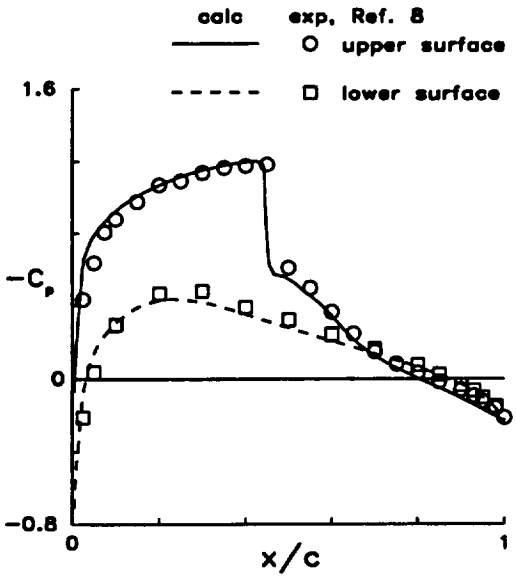

(a) pressure coefficient.

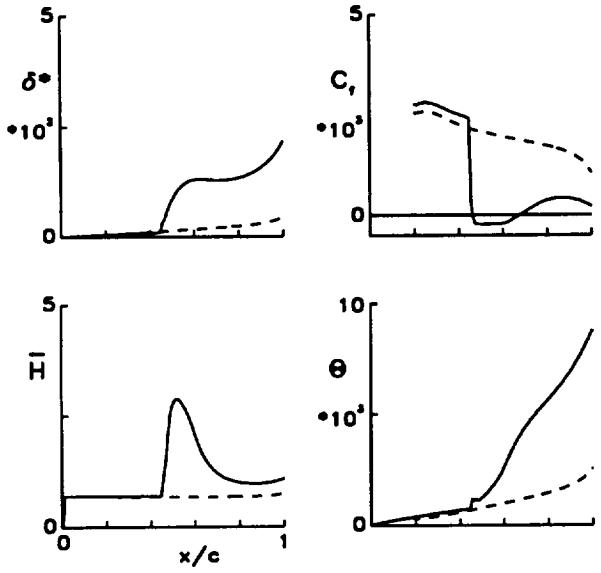

(b) boundary layer vaiables.

Fig. 3 Comparison of calculated and experimental results for NACA 0012 airfoil at M = 0.775, $\alpha = 2.05^\circ$, $Re_c = 10^7$.

For conditions below the buffet onset boundary, fully converged viscous solutions are obtained, including stable shock-induced separation bubbles as in Fig. 3. Since the boundary layer equations are quasi-steady, while the CAP—TSDV code is time accurate, it is not surprising that fully converged solutions cannot be obtained at each time step for conditions above the buffet onset boundary. The capability of the current coupling method must thus be evaluated based on agreement with experimental results and other calculations (see Ref. 32 for more details). Figures 4 and 6 indicate that the present method gives good agreement with experimental buffet onset and frequency. This is very encouaging, since it

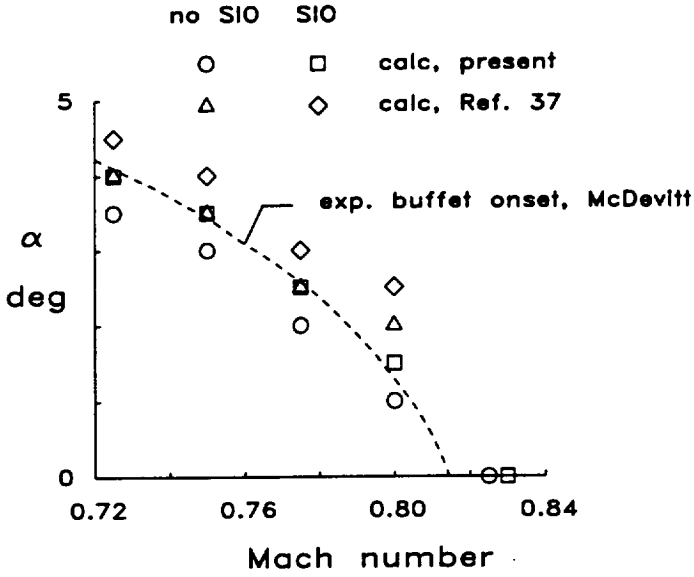

Fig. 4 Comparison of calculated and experimental buffet onset boundaries for the NACA 0012 airfoil.

is just such difficult computational conditions for which the coupling method is intended. Note particularly the ability of the method to achieve a significant penetration into the buffet region as seen in Fig. 6.

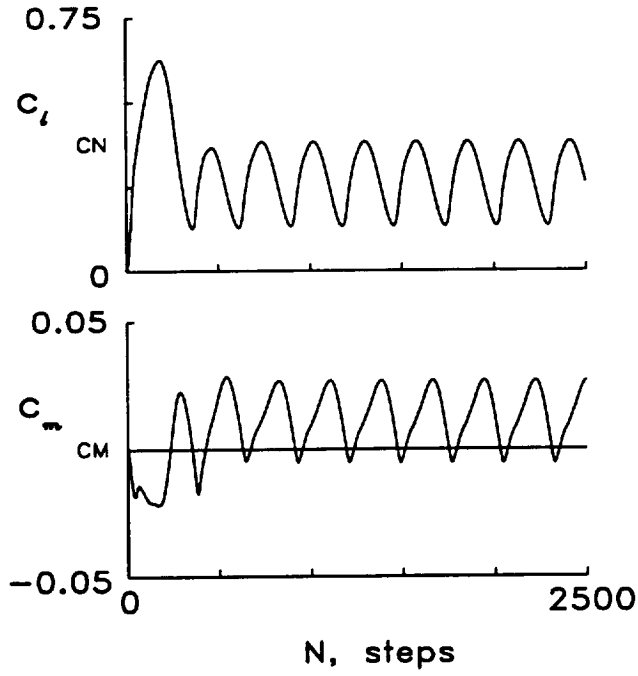

Fig. 5 Lift and moment coefficient time histories for the NACA 0012 airfoil at SIO conditions: M = 0.775, $\alpha = 4.0^\circ$, $Re_c = 10^7$.

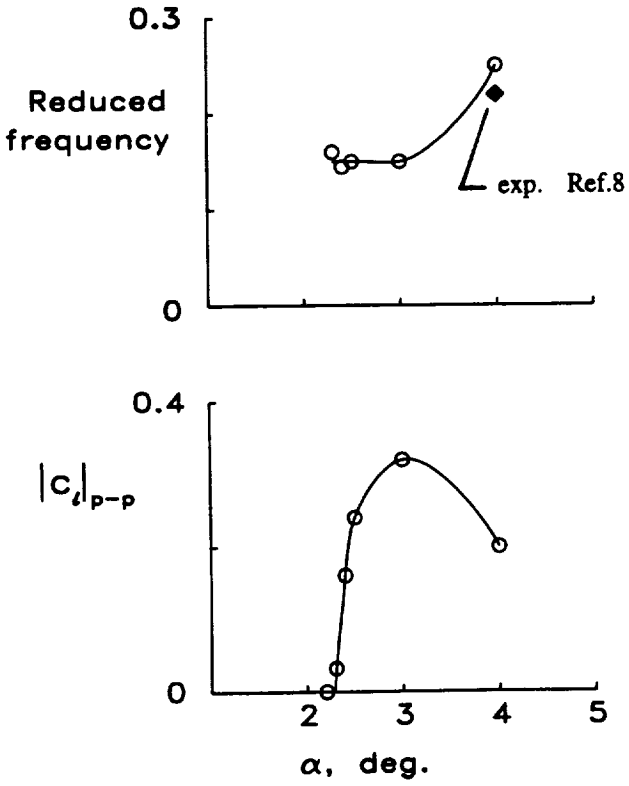

Fig. 6 Reduced frequency and amplitude of lift coefficient versus angle. NACA 0012 airfoil, M = 0.775, $Re_c = 10^7$.

Eighteen Percent Thick Circular Arc Airfoil Calculations

Numerous wind tunnel tests have reported SIO for the 18 percent thick circular arc airfoil. References 6 and 7 document SIO for $0.73 < M < 0.78$ and for Reynolds numbers from 1 to 17 million. Tests were conducted in a blow-down wind tunnel with walls contoured to simulate free air streamline conditions. The oscillations were at a characteristic frequency of $k_b \approx 0.47$,[6] varying little with Mach number, and decreasing slightly for nonzero angles. A sensitivity of the range of SIO was found for $Re_c \approx 1 - 6$ million. A significant feature is a hysteresis of the SIO phenomenon with regard to increasing or decreasing Mach numbers. A number of SIO calculations for this airfoil are discussed by Edwards and Thomas.[11] Successful SIO calculations for isolated Mach numbers have been made using Navier-Stokes codes[11, 12, 38] and a TSD code with an IBLM.[15] These Navier-Stokes results were all low in calculated SIO frequency, $k_b \approx 0.40$, while the TSD result was $k_b \approx 0.34$. More recent calculations[13, 14] show very good agreement with experiment.

Calculations have been made with the CAP-TSDV 2–D code for conditions encompassing the experimental SIO region up to $M = 0.78$. Effects of Mach number, integral coupling gain, grid size, wake modeling, and disturbance amplitude upon the SIO have been studied[32]. Unless otherwise noted, $dt = 0.025$, $Re_c = 10$ million, $K_\delta = 0.00015$, the IBLM was initiated at 10 percent chord, and 5 Newton iterations were performed at each time step.

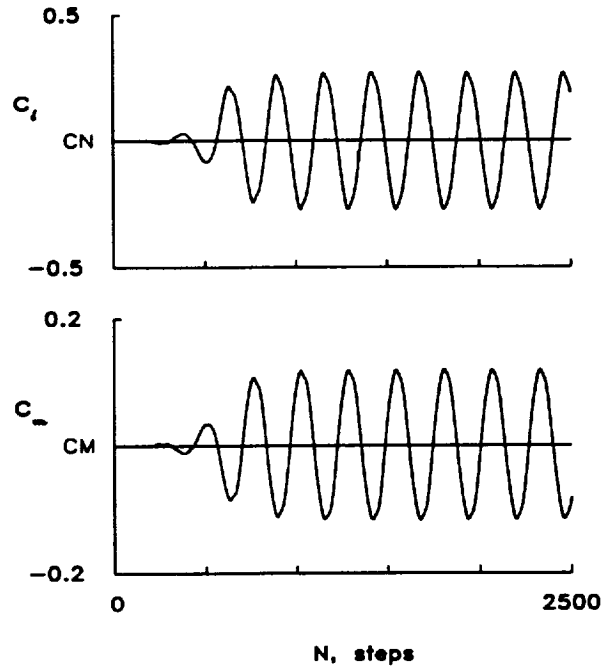

Fig. 7 Lift and moment coefficient time histories for the 18% thick circular arc airfoil at SIO conditions: M = 0.76, $Re_c = 10^7$.

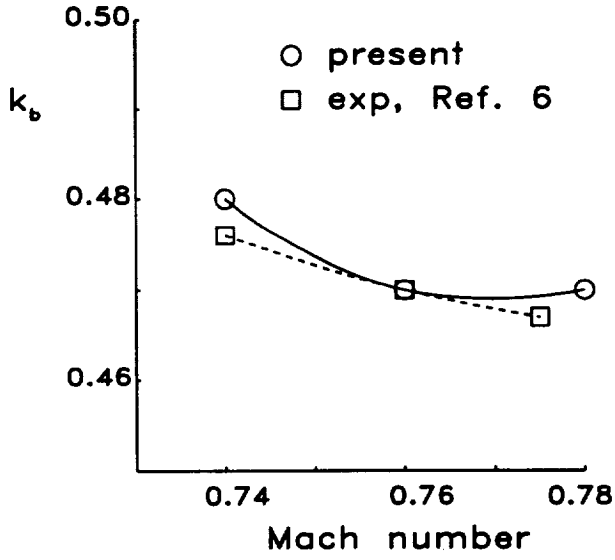

Fig. 8 Comparison of calculated and experimental SIO reduced frequencies for the 18% thick circular arc airfoil.

The buildup of the SIO at $M = 0.76$ from "zero" flow field conditions is shown in Fig. 7. The buildup of the SIO to its limit-amplitude occurs in three shock oscillation cycles over 2.5 chordlengths of travel. Comparison of Figures 4 and 7 indicates more nearly sinusoidal air-

loads for this case, involving upper and lower surface shocks oscillating antisymmetrically, than for the NACA 0012 airfoil case, which involves a single upper surface shock motion.

Calculated and experimental[6] reduced frequencies for these SIO are compared in Fig. 8. The calculated frequencies are in very good agreement with experiment, including the mild decrease in frequency with increasing Mach number.

The amplitude of the shock excursion is approximately 40 percent chord with the aftmost shock position increasing about 5 percent chord from $M = 0.74$ to 0.78. The displacement thickness at the trailing edge varies from 1.5–11 percent chord. All of the computed shocks are "strong" shocks as discussed by McDevitt[6] (supersonic-to-subsonic flow) with nearly constant subsonic pressure levels aft of the shocks to the trailing-edge. The forward motion of the shock for all three Mach numbers stalls just forward of the crest of the airfoil at midchord, coinciding with rising pressures aft of the shock and formation of a suction pressure region, leading to formation of the new shock. The computed shock speeds during their forward movement are quite constant, with speed increasing slightly with increasing Mach number. The increasing shock speed with Mach number, in conjunction with the larger shock excursion mentioned above leads to almost constant periods for the SIO. The gain used for these results, $K_\delta = 0.00015$, gives very good agreement[32] with the experimental SIO frequency of $k = 0.47$.

Wind tunnel tests[6,7] show an interesting hysteresis of the onset of the SIO phenomenon depending upon increasing or decreasing Mach number. The new coupling method is able to reproduce this effect. Figure 9 superimposes calculated SIO onset and quenching boundaries with those from Ref. 6. For increasing Mach number at $Re_c = 10$ million, SIO onset occurs for $M = 0.76$ experimentally and for $M = 0.755$ computationally. For decreasing Mach number, the SIO quenches for $M \approx 0.73$ experimentally and for $M = 0.735$ computationally. For lower Reynolds numbers, experimental results indicate a narrowing of the SIO region, presumably due to transition effects. The present calculations show an indication of such an effect of Reynolds number, although smaller in magnitude. No attempt has been made to modify the present method with transition modeling features.

Comparison of the SIO onset boundaries in Figs. 4 and 9 indicates that different mechanisms are operating in the two cases. Inspection of steady flow conditions occurring for increasing Mach numbers within the hysteresis region, $0.73 < M < 0.76$, confirms this to be the case. Figure 10 gives steady computed surface pressure and boundary layer parameters for $M = 0.74$. Trailing-edge separation at $x/c = 0.85$ is clearly evident. Also evident is the near separation at $x/c = 0.60$ induced by the shock-boundary layer interaction. This pattern of incipient shock-induced and trailing-edge flow separation offers an explanation of the SIO hysteresis for this airfoil. With increasing Mach number, separation initiates at the trailing-edge while the weak shock on the airfoil is not yet strong enough to separate the boundary layer. Investigation of boundary layer parameters (not shown) indicates the local minimum in the skin friction coefficient, C_f, observed just downstream of the shock decreases continuously with increasing Mach number. When this local minimum $C_f \approx 0$ at $M = 0.755$, the spontaneous SIO discussed above develop. With the SIO established, oscillations persist for decreasing Mach number until $M = 0.735$ where the minimum value (steady) of C_f at the shock is ≈ 0.0010.

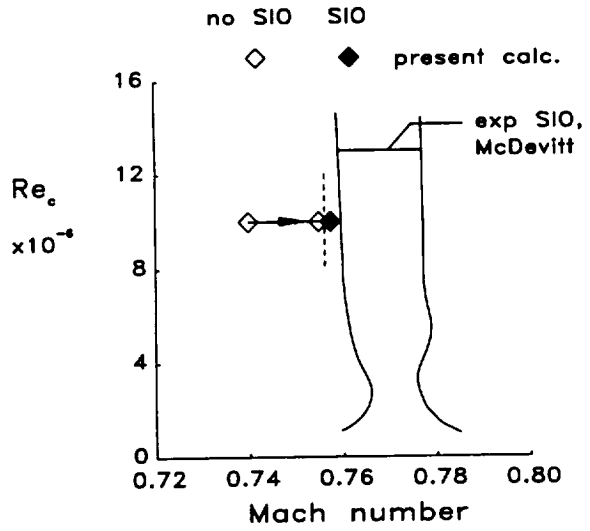

(a) increasing Mach number.

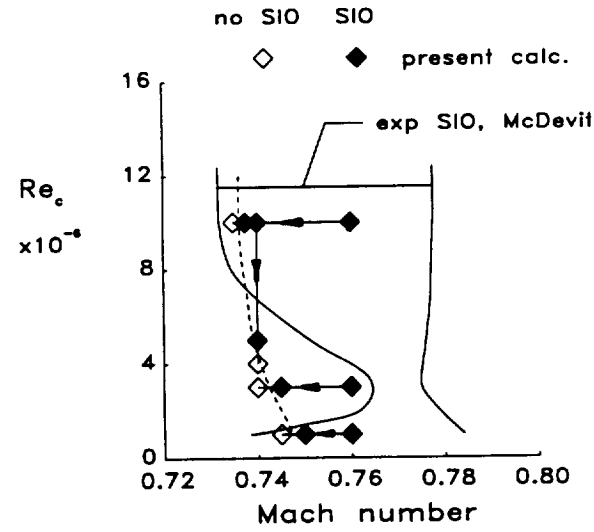

(b) decreasing Mach number.

Fig. 9 Regions of SIO for increasing and decreasing Mach number for the 18% thick circular arc airfoil.

The hysteresis of the SIO for $0.73 < M < 0.76$, coupled with the flow separation patterns discussed above suggests that oscillations might be induced, within this region, by appropriate perturbations. Figure 11 shows that this is indeed the case. For $M = 0.74$, perturbations were introduced by simulating trailing-edge control surface motions, δ_f (exponentially shaped pulses were used for the 1/4c flap). For $\delta_f < 10°$, stable decaying airload oscillations are seen, whereas the oscillations quickly lock onto the SIO waveform for $\delta_f > 10°$. Thus an amplitude threshold, jump phenomenon is identified as one of the SIO mechanisms for this airfoil.

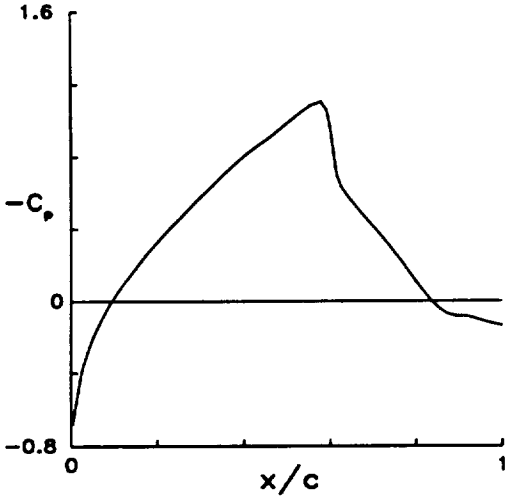

(a) pressure coefficient.

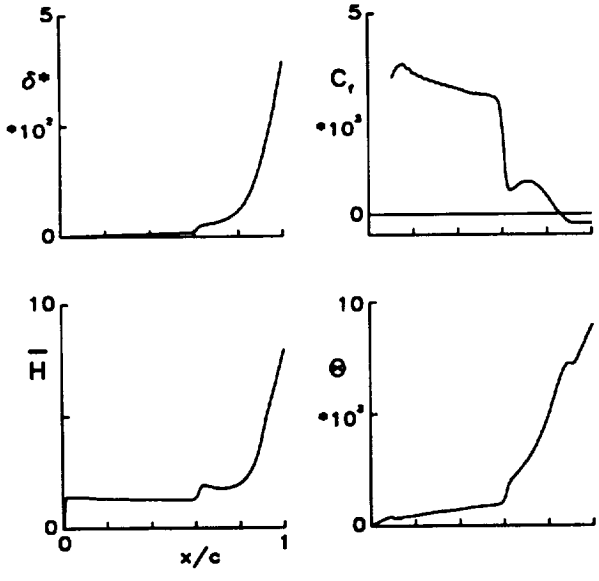

(b) boundary layer variables.

Fig. 10 Steady calculated results for the 18% thick circular arc airfoil within SIO hysteresis region, M = 0.74, $Re_c = 10^7$.

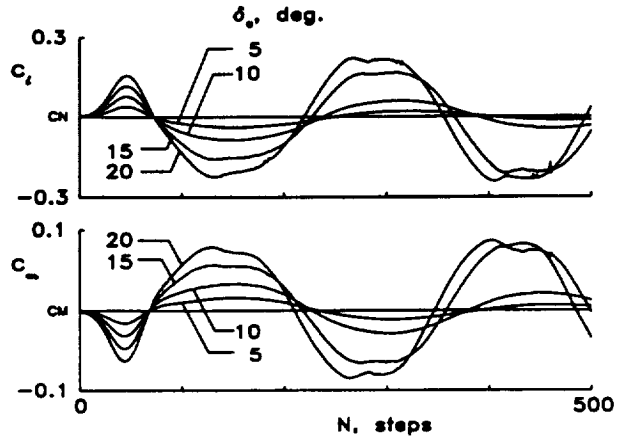

Fig. 11 Lift and moment time histories for the 18% thick circular arc airfoil exhibiting jump phenomenon due to flap pulses, M = 0.74.

Wing Flutter Models

The first wing flutter model, shown in Fig. 12, is the AGARD Standard Aeroelastic Configuration[39, 40] which was tested in the Transonic Dynamics Tunnel (TDT) at NASA Langley Research Center. It is a semispan wall-mounted model having a quarter-chord sweep angle of 45 deg., a panel aspect ratio of 1.65, and a taper ratio of 0.66. The wing had a NACA 65A004 airfoil sction and was constructed of laminated mahogany. The wing is modeled structurally using the first four natural vibration modes, with natural frequencies ranging from 9.6 Hz for the first bending mode to 91.54 Hz for the second torsion mode The CAP-TSDV calculations were performed on a 150 x 30 x 80 point computational grid with 100 points along each of 15 spanwise chords on the wing. Other computational conditions were: nondimensional time step $dt = 0.05$, one Newton iteration, and $K_\delta = 0.00030$.

The second wing flutter model, shown in Fig. 13, is a typical business jet configuration also tested in the TDT. The semispan wing-fuselage model was mounted on the wind tunnel sidewall and tested in air, with experimental flutter data obtained for Mach numbers from 0.628 to 0.888. The wing has a taper ratio of 0.29 and a midchord sweep of 23 degrees. The airfoil thickness varies from 13 percent at the symmetry plane (for the extended wing-alone configuration analyzed) to 8.5 percent at the wing tip. Six natural vibration modes were included in the calculations, with frequencies ranging from 4.3 Hz to 62.7 Hz. The CAP-TSDV calculations were performed on a 100 x 50 x 80 point computational grid with 45 points along each of 33 spanwise chords on the wing. Other computational conditions were: nondimensional time step $dt = 0.03$, one Newton iteration, and $K_\delta = 0.00010$.

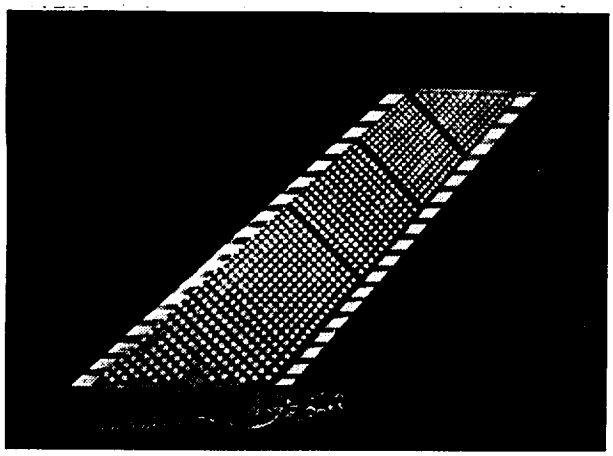

Fig. 12 Planview of AGARD Wing 445.6 Standard Aeroelastic Configuration.

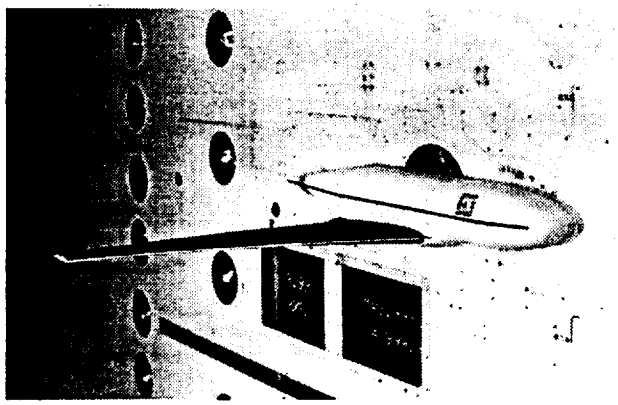

Fig. 13 Business jet flutter model mounted in NASA Langley Transonic Dynamics Tunnel.

AGARD Wing 445.6 Flutter Calculations

Model tested in air. The majority of published calculations for this model (actually a series of models with similar planforms) are for the "weakened model #3" tested in air, since this test covered the largest transonic speed range and showed a significant transonic dip effect. Figure 14 gives new results from CAP-TSDV (large square symbols) and includes results from other NASA Langley Research Center studies[41, 42] for comparison. It is informative to discuss these results with respect to two Mach number ranges.

— M < 1.0. The CAP-TSDV results for these four Mach numbers are in excellent agreement with experiment. The comparisons with other calculations illustrate details which appear to be relevant to such aeroelastic analysis (below Mach one) in general. As a point of reference, linear theory flutter calculations for this case[41] are also in very good ageement with the experimental points except for that at $M = 0.96$ where the calculation is unconservative. This is to be expected, since nonlinear transonic effects for this thin wing are confined to Mach numbers very near one. For the three lower Mach numbers, the CAP-TSDV and CFL3D-Euler[42] results are in excellent agreement. The inviscid calculations for $M = 0.901$ and 0.96 increasingly overpredict

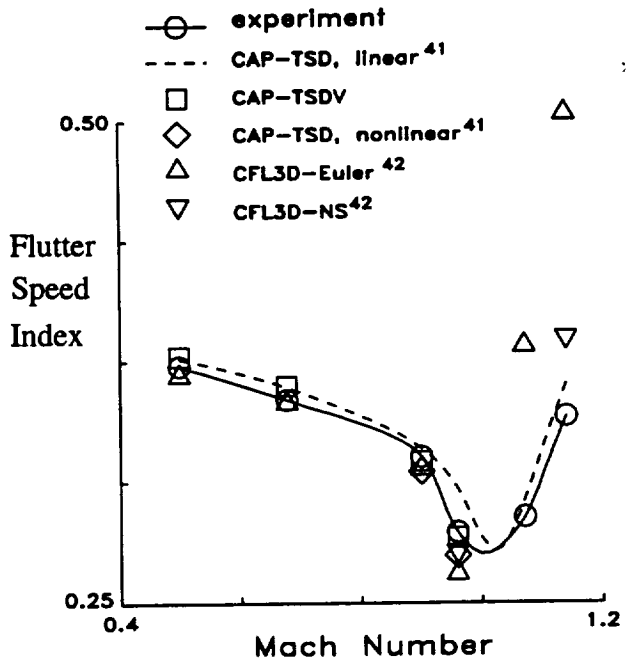

(a) flutter speed index.

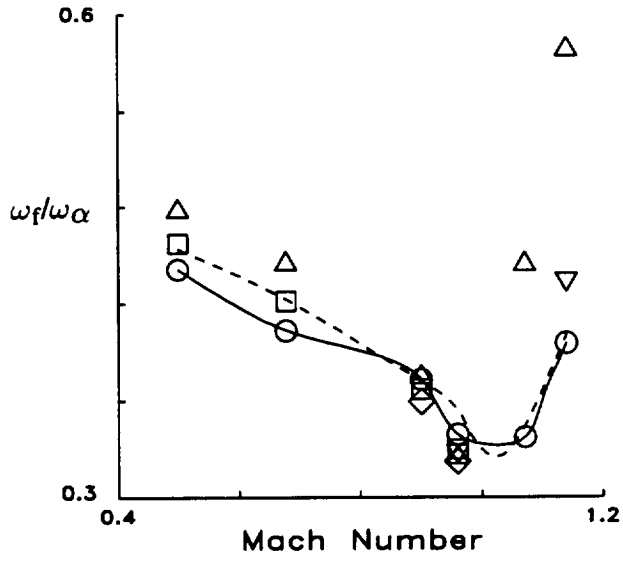

(b) frequency.

Fig. 14 Comparison between experimental and calculated flutter speed index and frequency for the AGARD Wing 445.6 tested in air.

the drop in the transonc flutter boundary. At $M = 0.96$ the two viscous calculations, from CAP-TSDV and the CFL3D-Navier-Stokes, indicate that viscous modeling is required to correct this overprediction. This effect appears to grow in importance for thicker wings, as will be seen below.

— M > 1.0. Fewer calculations have been published dealing with this very low supersonic Mach number range and the results summarized in figure 14 indicate that more work is needed to understand differences between experiment and calculation. Again, linear CAP-TSD results are in very good agreement with experiment. Higher level calculations have been less successful for these two low supersonic cases. The inviscid Euler equation results[42] are very unconservative and the viscous Navier-Stokes result corrects only 80 percent of the discrepancy at $M = 1.141$[42]. Invisid CAP-TSD results (not shown) are somewhat higher in flutter speed index than the Euler results and the effect of including the viscous boundary layer at $M = 1.141$ is less effective in correcting the discrepancy than that shown in Figure 14. A number of factors may be considered in discussing this discrepancy. The flutter boundary for this model is quite sensitive to Mach number here, as noted by the steep gradient seen in these two flutter points. In addition, none of the codes attempt to model the details of the cut-off tip of the model. Finally, for these very low supersonic Mach numbers, wind tunnel interference effects are not well understood.

Model tested in heavy gas. Since the above results for the model tested in air resulted in somewhat unrealistically large mass ratios and small reduced flutter frequencies, it was desirable to obtain results for the "weakened models #5 and #6" which were tested in heavy gas and had more reasonable ranges of mass ratio and frequency. CAP-TSDV calculations for these cases are shown in Fig. 15. Again, for these cases with $M \leq 1.0$, the CAP-TSDV results are in excellent agreement with experiment for $M = 0.74$ and 0.92. Due to issues discussed above for very low supersonic Mach numbers, calculation have not been attempted for the third experimental Mach number of 1.0. Instead calculations at $M = 0.94$, 0.95, and 0.96 revealed an interesting minimum feature in the flutter speed index parameter at $M = 0.95$. Further numerical experimentation at $M = 0.96$ revealed nonlinear response features. It was found that the estimated damping of the flutter mode was dependent upon amplitude. Figure 16 shows a simulated wing "tip rap" response for $M = 0.96$ and $Q = 0.75$ psi. The interpolated flutter dynamic pressure from the experimental data for this Mach number is $Q_f = 0.757$ psi. The early portion of the response indicates positive damping of the flutter mode and a higher frequency mode. The damping of the flutter mode decreases as the response amplitude decays to approximately 0.12 inches peak-to-peak, where stable limit cycle oscillations persist. This limit cycle behavior was further studied by sequentially increasing the dynamic pressure between computed runs from $Q = 0.5$ to 0.81 psi.. The resulting tip deflection time history is

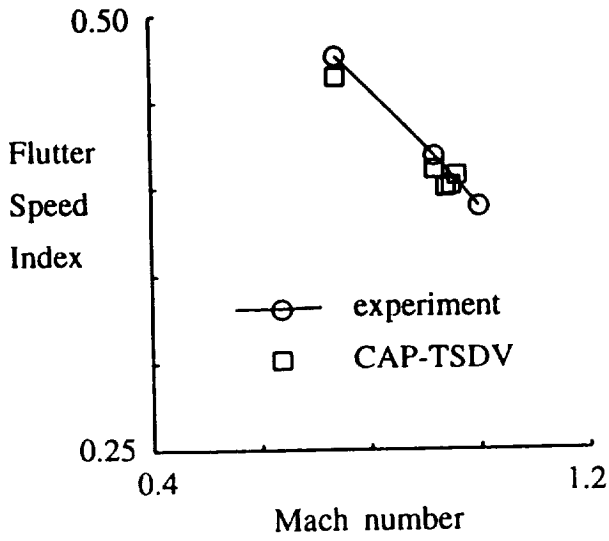

(a) flutter speed index.

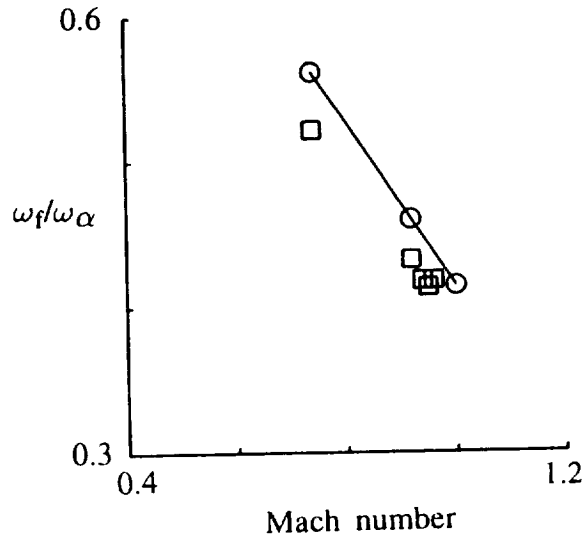

(b) frequency.

Fig. 15 Comparison between experimental and calculated flutter speed index and frequency for the AGARD Wing 445.6 tested in heavy gas.

shown in Figure 16. Eleven computer runs with a total of 22,000 time steps were calculated. The dynamic pressure was incremented as indicated in steps between restarted runs. For $Q \leq 0.60$ psi. the response is damped and for $Q = 0.70$ psi. small neutrally stable oscillations are seen. With Q increased to 0.78 psi. slowly divergent oscillations develop and with further increase to 0.81 psi. the divergent oscillations grow with increased negative damping until the amplitude reaches approximately 0.12 inches peak-to-peak. The growth of the oscillations then quenches and it appears that a limit cycle condition will

again develop, although further calculations are needed to fully establish this feature.

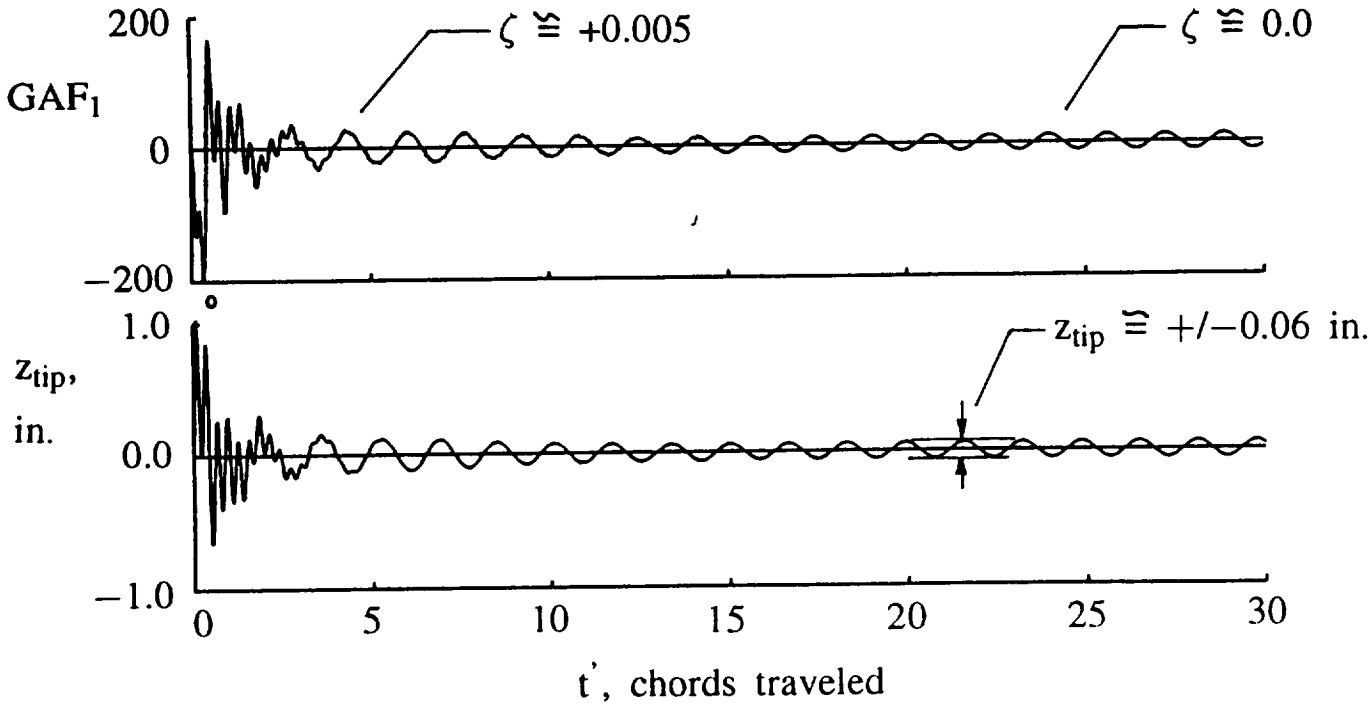

Fig. 16 Calculated AGARD Wing 445.6 tip response in heavy gas for M = 0.96 and Q = 0.75 psi.

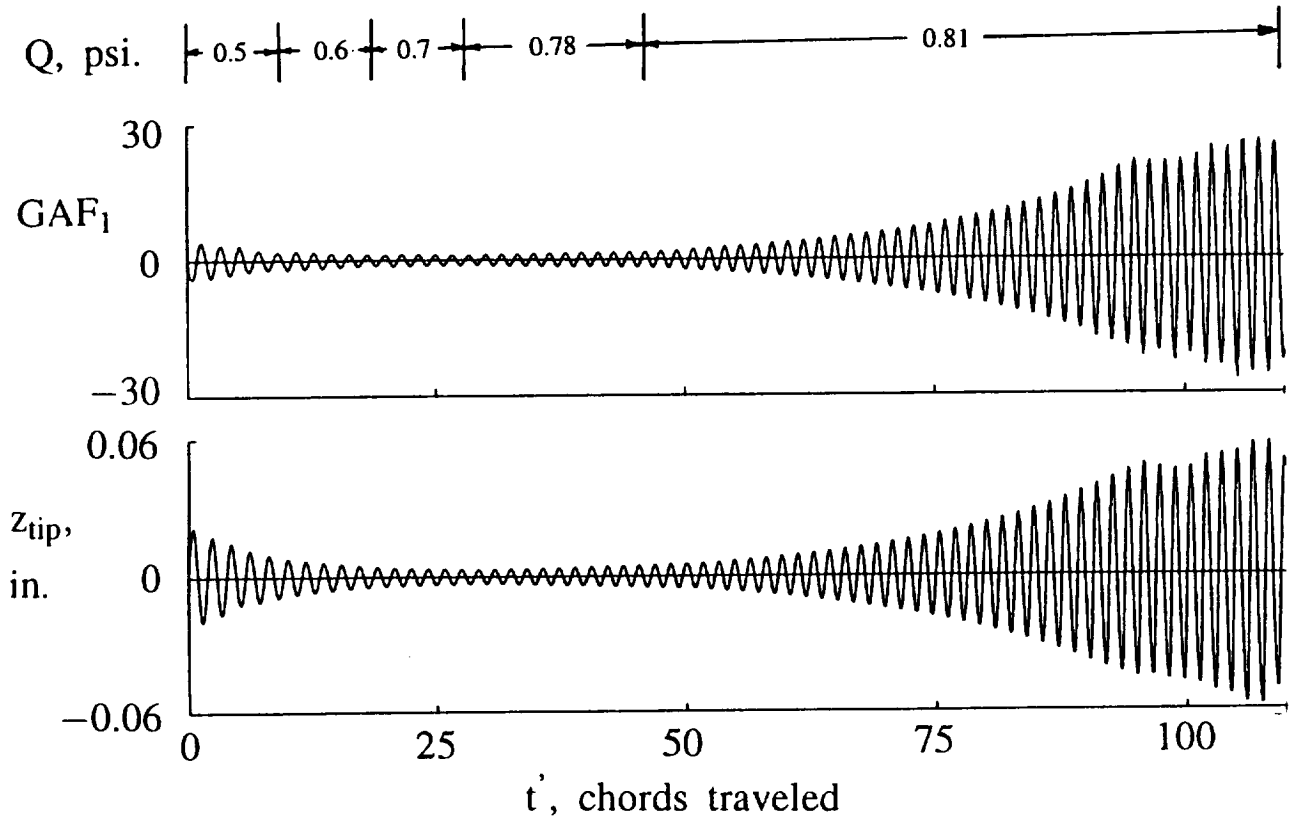

Fig. 17 Calculated AGARD Wing 445.6 response in heavy gas for M = 0.96 and increasing dynamic pressure.

This limit cycle behavior for this model was only observed for the highest calculated Mach number, $M = 0.96$ which lies on the "backside" of the small transonic dip seen in Fig. 15. At this Mach number and for the wing motions calculated, the flow is fully attached with no significant transonic features. The boundary layer coupling method performed well, with well-converged displacement thickness profiles. Numerical flow visualizations of the wing pressure surfaced details which are possibly key to this nonlinear response behavior. At this Mach number and for this thin wing significant regions of near sonic flow develop adjacent to the wing upper and lower surfaces as the wing oscillates. Very high frequency upstream moving pressure waves are seen in the visualizations which are consistent with forward propagating Mach waves. At a given point on the wing, the frequency of these pressure waves is 10–20 times the flutter mode frequency for this case. The amplitudes of these calculated limit cycles is small and and no mention of such behavior is reported[40]. It is unlikely that such small motions, even if present, would have been detected since they would have been heavily masked by the model response to tunnel turbulence.

Business Jet Wing Flutter Calculations

The business jet wing flutter model shown in Figure 4 was tested in the Transonic Dynamics Tunnel at NASA Langley Research Center. Gibbons[43] presents flutter calculations for the model including spatial and temporal convergence studies, and surface pressure coefficient comparisons for rigid and statically deformed cases, using TSD, Euler, and Navier-Stokes methods. For the present study, the effect of including viscous effects using the CAP-TSDV code was investigated.

The model was constructed from aluminum plate with fiberglass wrapped foam providing the airfoil contour. The wing was mounted low on the side-wall mounted fuselage model which had a circular cross-section with a conical aft end. The wing root angle-of-attack was varied during the test to minimize loading. The maximum angle needed for this purpose was 0.2 degrees at the highest tested Mach number. This root angle was used for the calculations described below. This resulted in calculated static tip deflections of -1.33 in. at $M = 0.628$ and $+1.35$ in. at $M = 0.888$. The Reynolds numbers for these two Mach numbers were 2.17 million and 1.14 million respectively, based on the 2.0 ft. root chord. The model had a 4.4 ft. semispan.

Contour plots of the upper and lower wing surface pressure, displacement thickness, and skin friction are shown in Fig. 18 for $M = 0.888$. Note the lower surface leading edge suction peak and mild inboard shock seen in the Fig. 18a. The lower surface displacement thickness is similar to the upper surface with maximum thicknesses below one percent except near the root where the lower surface shock produces a thickness of approximately 1.5 percent root chord. The skin friction in Fig. 18c. reflects these features seen in the displacement thickness and is informative regarding closeness to separation. The lower surface trailing-edge is separated at the root and there is small separation bubble just inboard of the tip and aft of the leading-edge suction peak. The skin friction coefficient is low in the trailing-edge region of the upper surface, reaching a minimum near 88 percent span. This region and the lower surface separation bubble are key in the effect of amplitude upon flutter mode response described below.

Calculated flutter speed indices and frequencies versus Mach number are compared with experiment in Fig. 19. The linear CAP-TSD, Euler, and Navier-Stokes resultes are from Gibbons[43] while the four CAP-TSDV data points are new. Comparison of these flutter boundaries leads to similar observations as for the 445.6 wing:

1. Inviscid calculations agree among themselves and are in very good agreement with experiment for the lower Mach numbers. For higher Mach numbers in the vicinity of the transonic dip region, the inviscid codes become increasingly conservative. For this wing, inviscid calculations should not be used for $M > 0.80$.

2. For Mach numbers at and below the minimum transonic flutter speed index, the viscous methods, CAP-TSDV and CFL-3D are in agreement and both provide good agreement with experiment, largely correcting the deficiency in the inviscid methods. Also, the finite element structural model was not updated with information from the model vibration testing. This may account for a significant portion of the remaining differences between experiment and the calculations.

3. Linear flutter calculations[43] are in excellent agreement with experiment up to $M = 0.85$, but cannot be relied upon for higher transonic Mach numbers. The good agreement in the lower transonic speed range is due to well-known compensating defects of linear theory wherein thickness and viscous effects are neglected.

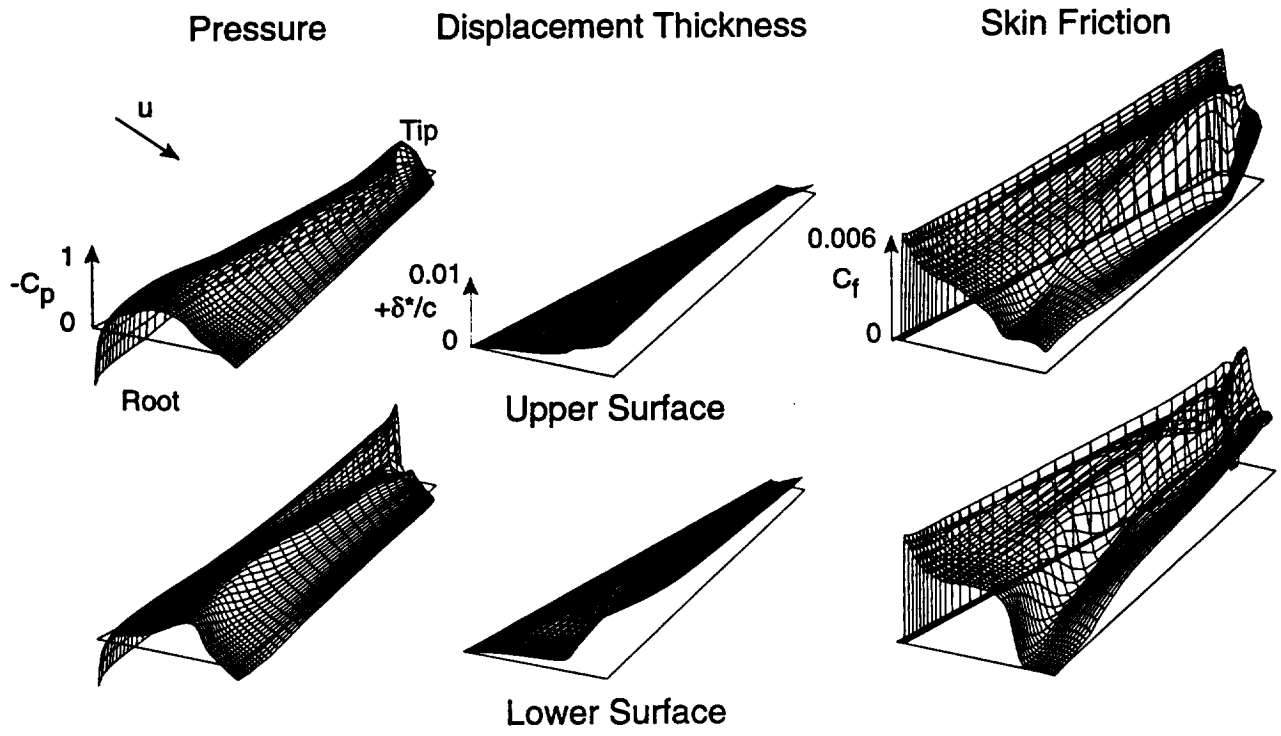

Fig. 18 Contour plots of business jet wing pressure and boundary layer parameters at statically deformed conditions: M = 0.888, Q = 79 psf., α = 0.2°, Re_c = 1.14 million.

All of the results discussed thus far were obtained from transient or harmonic responses of small amplitude, that is, wing tip response amplitudes were less than several tenths of an inch. Under these conditions, no large changes of the static aerodynamic loading occurred and transient responses exhibited exponential stability, characteristic of a "locally linear" system behavior. At $M = 0.888$ the CAP-TSDV code was able to calculate large amplitude response motions which demonstrated limit cycle behavior. The motion was calculated for the experimental flutter dynamic pressure of 79 lb/ft^2. The conditions for the limit cycle are noted in Fig. 19 by the solid symbol indicating a 0.5 Hz. increase in frequency over the small amplitude value. Figure 20 shows two transient responses confirming the limit cycle behavior. The motions were excited from converged statically deformed conditions by multiplying the modal displacements and velocities by factors of 5.0 for Fig. 20a and 0.5 for Fig. 20b. The larger factor simulates a wing tip displacement of about 7 inches, resulting in decaying oscillations to a limit cycle with an amplitude of 5–6 inches peak-to-peak. The smaller factor results in oscillations growing in amplitude to the limit cycle. This behavior is similar to model behavior observed during the test. Video tape of the model motions at the experimental "flutter" conditions for this Mach number shows the model to be undergoing constant amplitude wing oscillations with amplitude of slightly less than one tip chord (6.3 inches) peak-to-peak. This is in very good agreement with the calculated LCO amplitude and frequency shown in Fig. 20. The plate construction of the model provides sufficient strength to allow the model to sustain oscillations of this amplitude without structural failure. Inspection of the wing boundary layer parameters and surface pressures during the calculated limit cycle oscillations confirmed that the flow over the wing was intermittently separating and reattaching in the outboard upper and lower surface regions described above. This apparently provides the mechanism needed to quench the growth of the unstable flutter mode motions.

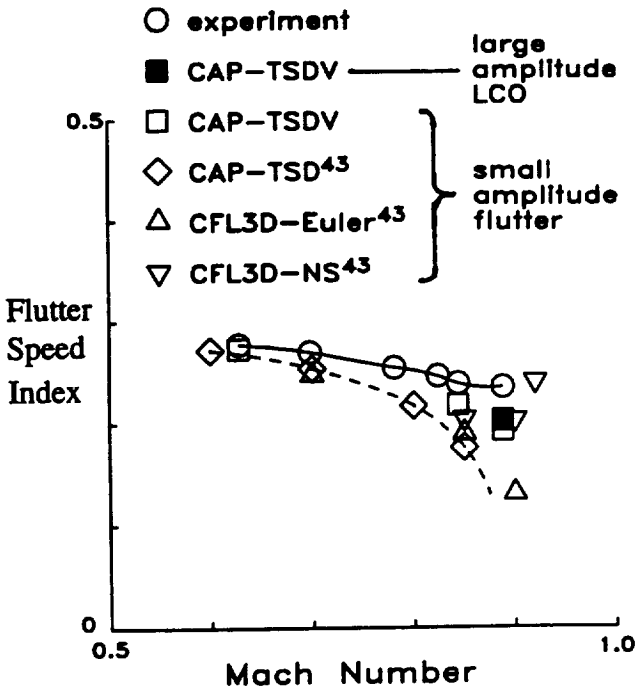

(a) flutter speed index.

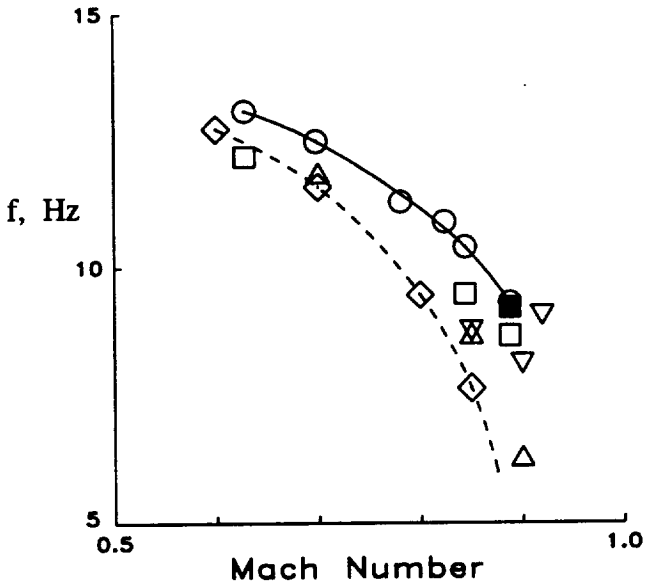

(b) frequency.

Fig. 19 Comparison between experimental and calculated flutter speed index and frequency for a business jet flutter model tested in air.

Concluding Remarks

A viscous-inviscid interactive coupling method has been described, directed towards the computation of unsteady separating and reattaching transonic flows which must be treated in cases of self-excited shock-induced oscillations and transonic flutter. Lag-entrainment integral boundary layer equations and a transonic small disturbance potential code are coupled with a variable gain, integral control coupling method. The buffet onset boundary for the NACA 0012 airfoil is shown computationally to be a Hopf bifurcation and good agreement with experiment is shown for the boundary and oscillation frequencies. For the 18 percent thick circular arc airfoil, very good agreement with experiment is shown for shock oscillation frequencies. The hysteresis with Mach number of the oscillation onset boundary is reproduced computationally, including an amplitude threshold, jump phenomenon stability boundary.

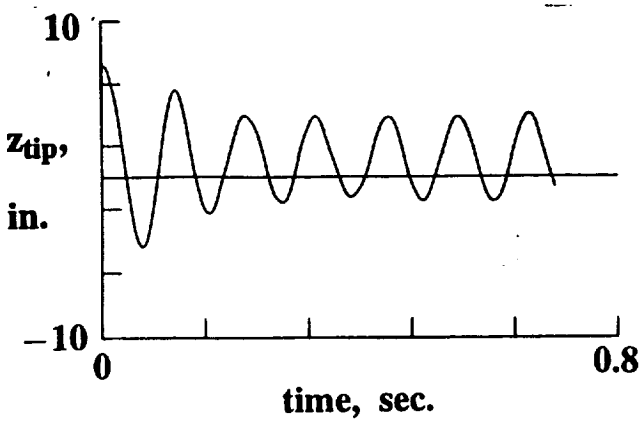

(a) amplitude decaying to limit cycle oscillation.

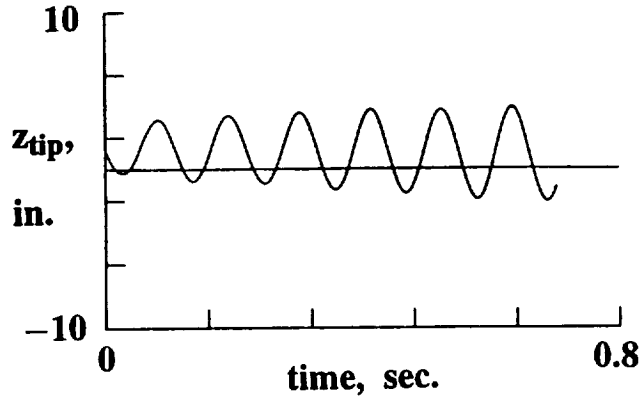

(b) amplitude growing to limit cycle oscillation.

Fig. 20 Calculated limit cycle response for a business jet wing flutter model: M = 0.888, Q = 79 psf., Re_c = 1.14 million.

Flutter calculations for the AGARD 445.6 flutter model are in excellent agreement with experiment for $M < 1.0$ for models tested in air and heavy gas. Calculations with the CAP-TSDV code are in excellent agreement with results from a Navier-Stokes code at $M = 0.96$. For Mach numbers below and very near unity, viscous modeling is required for such thin wings in order to achieve acceptable accuracy. In this region, calculations show evidence of small amplitude limit cycle behavior. For very low supersonic Mach numbers,

agreement with experiment is not yet satisfactory. Improved modeling and/or knowledge of wind tunnel test conditions is needed.

Flutter calculations for a business jet wing model also show very good agreement with experiment for the available test data up to $M = 0.9$. For this thicker wing, the requirement for viscous modeling extends to lower transonic Mach numbers. Again, calculations with the CAP-TSDV code are in very good agreement with a Navier-Stokes code at $M = 0.888$ for small amplitude flutter motions. For large amplitude wing oscillations, the CAP-TSDV code predicts limit cycle behavior in very good agreement with that observed during wind tunnel tests of the model.

Acknowledgement

The author would like to express his appreciation to Donald F. Keller of the Aeroelasticity Branch, NASA Langley Research Center, for valuable discussion regarding the wind tunnel test of the business jet flutter model. Great appreciation is also due Michael D. Gibbons, Lockheed Engineering & Sciences Corp., for valuable discussions of his experience with flutter calculations for that model. His Reference 43, published posthumously, should be used as a model of careful and accurate computational aeroelasticity.

References

1. Cunningham, A. M., "Practical Problems: Airplanes," Chapter 2 in Unsteady Transonic Aerodynamics, ed. by D. Nixon, Vol. 120 in AIAA Progress in Aeronautics and Astronautics, 1989.
2. Mabey, D. G., "Physical Phenomena Associated with Unsteady Transonic Flow," Chapter 1 in Unsteady Transonic Aerodynamics, ed. by D. Nixon, Vol. 120 in AIAA Progress in Aeronautics and Astronautics, 1989.
3. Eckstrom, C. V., Seidel, D. A., and Sandford, M. C., "Unsteady Pressure and Structural Response Measurements on an Elastic Supercritical Wing," AIAA Paper 88-2277, April 1988.
4. Edwards, J. W., and Malone, J. B., "Current Status of Computational Methods for Transonic Unsteady Aerodynamic and Aeroelastic Applications," Paper No. 1 in Transonic Unsteady Aerodynamics and Aeroelasticity, AGARD CP 507, March 1992.
5. Edwards, J. W., "Technical Evaluation Report on 1991 Specialists' Meeting on Transonic Unsteady Aerodynamics and Aeroelasticity." Paper T in Transonic Unsteady Aerodynamics and Aeroelasticity, AGARD CP 507, March 1992.
6. McDevitt, J. B., "Supercritical Flow About a Thick Circular-Arc Airfoil," NASA TM-78549, Jan. 1979.
7. McDevitt, J. B., Levy, L. L., Jr., and Deiwert, G. S., "Transonic Flow About a Thick Circular-Arc Airfoil," *AIAA Journal*, Vol. 14, May 1976, pp. 606–613.
8. McDevitt, J. B., and Okuno, A. F., "Static and Dynamic Pressure Measurements on a NACA 0012 Airfoil in the Ames High Reynolds Number Facility," NASA TP-2485, June 1985.
9. Lee, B. H. K., "Oscillatory Shock Motion Caused by Transonic Shock Boundary-Layer Interaction," *AIAA Journal*, Vol. 28, pp. 942–944.
10. Hirose, N., and Miwa, H., "Computational and Experimental Research on Buffet Phenomena of Transonic Airfoils," NAL TR-996T, 1988.
11. Edwards, J. W., and Thomas, J. L., "Computational Methods for Unsteady Transonic Flows," Chapter 5 in Unsteady Transonic Aerodynamics, ed. by D. Nixon, Vol. 120 in AIAA Progress in Aeronautics and Astronautics, 1989.
12. Levy, L. L., Jr., "Experimental and Computational Steady and Unsteady Transonic Flows About a Thick Airfoil," *AIAA Journal*, Vol. 16, June 1978, pp. 564–572.
13. Rumsey, C. L., Sanetrik, M. D., Biedron, R. T., Melson, N. D., and Parlette, E. B., "Efficiency and Accuracy of Time-Accurate Turbulent Navier-Stokes Computations," AIAA Paper 95–1835, June 1995.
14. Bartels, R. E., "Interactive Boundary Layer Computations Using the Improved k-ω Turbulence Model," Proc. of the 9th International Conference on Numerical Methods in Laminar and Turbulent Flow, Pineridge Press 1995.
15. Bartels, R. E., and Rothmayer, A. P., "An IBL Approach to Multiscaled Shock Induced Oscillation," AIAA Paper 95–2157, June 1995.
16. Green, J. E., Weeks, D. J., and Brooman, J. W. F., "Prediction of Turbulent Boundary Layers and Wakes in Compressible Flow by a Lag-Entrainment Method," R & M No. 3791, British Aeronautical Research Council, 1977.
17. Carter, J. E., "A New Boundary-Layer Inviscid Iteration Technique for Separated Flows," AIAA Paper 79-1450, July 1979.
18. Melnik, R. E., and Brook, J. W., "The Computation of Viscid/Inviscid Interaction on Airfoils With Separated Flow," Third Symposium on Numerical and Physical Aspects of Aerodynamic Flows, California State University, 1985, pp. 1-21–1-37.
19. LeBalleur, J. C., and Girodroux-Lavigne, P., "A Viscous-Inviscid Interaction Method for Computing Unsteady Transonic Separation," Third Symposium on Numerical and Physical Aspects of Aerodynamic Flows, California State University, 1985, (ONERA T. P. No. 1985-5)
20. Houwink, R., and Veldman, A. E. P., "Steady and Unsteady Separated Flow Computations for Transonic Airfoils," AIAA Paper 84-1618, June 1984.

21. Houwink, R., "Computation of Unsteady Turbulent Boundary Layer Effects on Unsteady Flow About Airfoils," Fourth Symposium on Numerical and Physical Aspects of Aerodynamic flows, Jan. 1989 (also NLR TP 89003 U).
22. Thomas, J. L., "Transonic Viscous-Inviscid Interaction Using Euler and Inverse Boundary-Layer Equations," Ph.D. Diss., Mississippi State Univ., Dec. 1983.
23. Holst, T. L., "Viscous Transonic Airfoil Workshop Compendium of Results," *Journal of Aircraft*, Vol. 25, Dec. 1988.
24. Chang, K. C., Alemdarogula, N., Mehta, U., and Cebeci, T., "Further Comparisons of Interactive Boundary-Layer and Thin-Layer Navier-Stokes Procedures," *Journal of Aircraft*, Vol. 25, Oct. 1988, pp. 89–903.
25. Drela, M., and Giles, M. B., "Viscous-Inviscid Analysis of Transonic and Low Reynolds Number Airfoils," *AIAA Journal*, Vol. 25, Oct. 1987, pp. 1347–1355.
26. Fenno, C. C., Jr., Newman, P. A., and Hassan, H. A., "Unsteady Viscous-Inviscid Interaction Procedures for Transonic Airfoils Using Cartesian Grids," *Journal of Aircraft*, Vol. 26, Aug. 1989, pp. 723–730.
27. Kusunose, K., Wigton, L., and Meredith, P., "A Rapidly Converging Viscous/Inviscid Code for Multi-Element Airfoil Configurations," AIAA Paper 91-0177, Jan. 1991.
28. Howlett, J. T., "Efficient Self-Consistent Viscous Inviscid Solution for Unsteady Transonic Flow", *Journal of Aircraft*, Vol. 24, Nov. 1987, pp. 737–744.
29. Batina, J. T., "Unsteady Transonic Algorithm Improvements for Realistic Aircraft Configurations," *Journal of Aircraft*, Vol. 26, Feb. 1989, pp. 131–139.
30. Rizzetta, D. P., "Procedures for the Computation of Unsteady Transonic Flows Including Viscous Effects", NASA CR-155249, Jan. 1982.
31. Howlett, J. T., "Calculation of Unsteady Transonic Flows With Mild Separation by Viscous-Inviscid Interaction," NASA TP-3197, June 1992.
32. Edwards, J. W., "Transonic Shock Oscillations Calculated with a New Interactive Boundary Layer Coupling Method," AIAA Paper 93–0777, January 1993.
33. Batina, J. T., "Unsteady Transonic Small-Disturbance Theory Including Entropy and Vorticity Effects," *Journal of Aircraft*, Vol. 26, June 1989, pp. 531–538.
34. Bennett, R. M., and Batina, J. T., "Application of the CAP-TSD Unsteady Transonic Small Disturbance Program to Wing Flutter," Proceedings—European Forum on Aeroelasticity and Structural Dynamics 1989, DGLR-Bericht 89-01.
35. Pitt, D. M., and Fuglsang, D. F., "Aeroelastic Calculations for Fighter Aircraft Using the Transonic Small Disturbance Equation," Paper No. 16 in Transonic Unsteady Aerodynamics and Aeroelasticity, AGARD CP 507, March 1992.
36. Batina, J. T., "A Finite-Difference Approximate-Factorization Algorithm for Solution of the Unsteady Transonic Small-Disturbance Equation," NASA TP 3129, January 1992.
37. Girodroux-Lavigne, P., and LeBalleur, J. C., "Time Consistent Computation of Transonic Buffet Over Airfoils," ICAS Paper No. 88-5.5.2, Sept. 1988, (ONERA TP No. 1988-97).
38. Steger, J. L., "Implicit Finite-Difference Simulation of Flow about Arbitrary Two-Dimensional Geometries," *AIAA Journal*, Vol. 16, July 1978, pp. 679–686.
39. Yates, E. C., Jr., "AGARD Standard Aeroelastic Configurations for Dynamic Response. Candidate Configuration I. — Wing 445.6," NASA TM 100492, August 1987.
40. Yates, E. C., Jr., Land, N. S., and Foughner, J. T., Jr., "Measured and Calculated Subsonic and Transonic Flutter Characteristics of a 45 Degree Sweptback Wing Planform in Air and in Freon-12 in the Langley Transonic Dynamics Tunnel," NASA TN D-1616, March 1963.
41. Cunningham, H. J., Batina, J. T., and Bennett, R. M., "Modern Wing Flutter Analysis by Computational Fluid Dynamics Methods," Journal of Aircraft, vol. 25, no. 10, pp. 962–968, 1988.
42. Lee-Rausch, E. M. and Batina, J. T., "Calculation of AGARD Wing 445.6 Flutter Using Navier-Stokes Aerodynamics," AIAA Paper 93–3476, August 1993.
43. Gibbons, M. D., "Aeroelastic Calculations Using CFD for a Typical Business Jet Model," NASA CR 4753, September 1996.